

NEGATIVE TERAHERTZ CONDUCTIVITY IN REMOTELY DOPED GRAPHENE BILAYER HETEROSTRUCTURES

V. Ryzhii,^{1,2} M. Ryzhii,³ V. Mitin,⁴ M. S. Shur,⁵ and T. Otsuji¹

¹ *Research Institute of Electrical Communication, Tohoku University, Sendai 980-8577, Japan*

² *Institute of Ultra High Frequency Semiconductor Electronics of RAS,
and Center for Photonics and Infrared Engineering,
Bauman Moscow State Technical University, Moscow 111005, Russia*

³ *Department of Computer Science and Engineering,
University of Aizu, Aizu-Wakamatsu 965-8580, Japan*

⁴ *Department of Electrical Engineering, University at Buffalo, SUNY, Buffalo, New York 1460-1920, USA*

⁵ *Departments of Electrical, Electronics, and Systems Engineering and Physics,
Applied Physics, and Astronomy, Rensselaer Polytechnic Institute, Troy, NY 12180, USA*

Injection or optical generation of electrons and holes in graphene bilayers (GBLs) can result in the interband population inversion enabling the terahertz (THz) radiation lasing. The intraband radiative processes compete with the interband transitions. We demonstrate that remote doping enhances the indirect interband generation of photons in the proposed GBL heterostructures. Therefore such remote doping helps surpassing the intraband (Drude) absorption and results in large absolute values of the negative dynamic THz conductivity in a wide range of frequencies at elevated (including room) temperatures. The remotely doped GBL heterostructure THz lasers are expected to achieve higher THz gain compared to previously proposed GBL-based THz lasers.

Keywords: graphene bilayer, population inversion, terahertz radiation

PACS: 72.80Vp, 78.67W, 68.65Pq

I. INTRODUCTION

The population inversion created by injection or optical pumping in graphene layers (GLs) and graphene bilayers (GBLs) [1] results in the negative dynamic conductivity in the terahertz (THz) range of frequencies [2, 3] and enables the graphene-based THz lasers [2–5]. Different research groups have demonstrated the THz gain in the pumped GLs [6–17] (see, also Ref. [17]). GLs and GBLs can serve as the active regions of the THz lasers with the Fabry-Perot resonators, dielectric waveguides, slot-lines including the plasmonic lasers [8, 19–24]. The GL and GBL heterostructure lasers can operate in a wide frequency range, including the 6 to 10 THz range, where using materials like A_3B_5 is hindered by the optical phonon effects [25–27]. The THz lasing in GL and GBL structures is possible if the contribution of the interband radiative transitions to the real part of the dynamic conductivity $\text{Re } \sigma$ in a certain range of frequencies surpasses the contribution of the intraband radiative processes associated with the Drude losses. The interband transitions include the direct (with the conservation of the electron momenta) and the indirect transitions (accompanied with the variation of the electron momentum due to scattering). The limitations imposed by the momentum and energy conservation laws allow only for the indirect intraband radiative transitions. In the GLs and GBLs with sufficiently long carrier momentum relaxation time τ , the direct interband radiative transitions dominate over the indirect intraband transitions and $\text{Re } \sigma < 0$. Recently [28, 29], we demonstrated that in GLs and GBLs with primarily long-range disorder scattering, the indirect interband transitions can prevail over the indirect intraband transitions leading to fairly

large absolute values of the negative conductivity $|\text{Re } \sigma|$. These values could exceed the fundamental limits for the direct transitions, which are $\sigma_Q = e^2/4\hbar$ for GLs and $2\sigma_Q$ for GBLs [1] (here e is the electron charge and \hbar is the Planck constant). As a result, in the GL and GBL structures with a long-range disorder one can expect that the condition $\text{Re } \sigma < 0$ could be fulfilled in a wider range of the THz frequencies, including the low boundary of the THz range. When the momentum relaxation is associated with long-range scattering mechanism, moderate values of τ might be sufficient for achieving $\text{Re } \sigma < 0$, especially in GBLs where the density of states (DoS) $\rho(\varepsilon)$ as a function of energy ε near the band edges ($\rho(\varepsilon) \simeq \text{const}$) in the latter is considerably larger than in GLs (where $\rho(\varepsilon) \propto |\varepsilon|$).

This paper deals with the GBL heterostructures with a remote impurity layer (RIL) located at some distance from the GBL plane and incorporating donors and acceptors or donor and acceptor clusters. We consider the GBL-RIL heterostructure as an active region of an injection THz laser. We show that the electron and hole injection from the side n- and p-contact regions into the GBL-RIL heterostructures leads to the population inversion enabling the enhanced negative dynamic conductivity, which, in turn, can result in lasing in the THz range. Figure 1 shows the schematic view of an injection laser based on the GBL-RIL heterostructure at the reverse bias voltage V . The remote (selective) doping can markedly affect the scattering of electrons and holes (see, for example [30, 31]) and, hence, the indirect radiative transitions. The GL and GBL heterostructures using remote doping were already fabricated and used for device applications [32, 33]. The heterostructures with the selectively doped GBL and RIL demonstrate the follow-

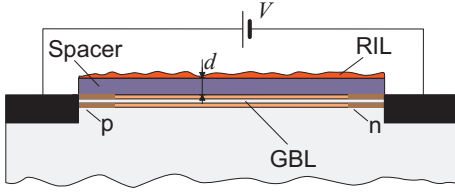


FIG. 1: Schematic view of an injection laser based on GBL-RIL heterostructure with the GBL doped with acceptors and the RIL doped with both donors and acceptors and with the chemically doped n- and p- injectors.

ing distinct features. First, the net electron and hole densities determined by both the pumping and RIL and the electron and hole quasi-Fermi energies, $\varepsilon_{F,e}$ and $\varepsilon_{F,h}$, are generally not equal. Second, relatively large scale of the donor and acceptor density fluctuations result in smooth (long-range) spatial variations of the potential in the GBL created by the RIL, separated by distance d from the GBL. This could result in the electron and hole scattering with a relatively small momentum change and, consequently, increase in the contribution of the indirect interband transitions in comparison with the interband transitions. Thus, the main role of the RIL is not to induce extra carrier in the GBL (as in high-electron mobility transistors) but to provide the specific mechanism of the electron and hole scattering reinforcing the indirect interband radiative transitions. We calculate the spectral characteristics of real part of the dynamic conductivity $\text{Re } \sigma$ in the pumped GBL-RIL heterostructures as a functions of the doping level and the spacer thickness d and compare the obtained characteristics with those of the undoped heterostructures. This analysis reveals the conditions for the selective doping enabling the negative dynamic conductivity in a wide frequency range, including the frequencies of a few THz. This might open new prospects of GBL heterostructures for the efficient THz lasers based on the GBL heterostructures.

II. DEVICE MODEL

We study the GBL-RIL heterostructures pumped via the injection from the side p- and n- contacts shown in Fig. 1. In the very clean pumped GBLs (or GLs) with a fairly high carrier mobility the intraband (Drude absorption) at the radiation frequencies above one THz should not play a dominant role. Hence, adding the selective doping might not be needed. However, in the GBLs with a relatively low carrier mobility caused by unavoidable (residual) charge impurities and imperfections, the RIL induced scattering could result in a substantial compensation of the Drude absorption and, therefore, enhancement of the negative dynamic conductivity. In the following, for definiteness, we consider the GBL-RIL heterostructures with the GBL doped with acceptors (with the density Σ_A) and the RIL formed by partially com-

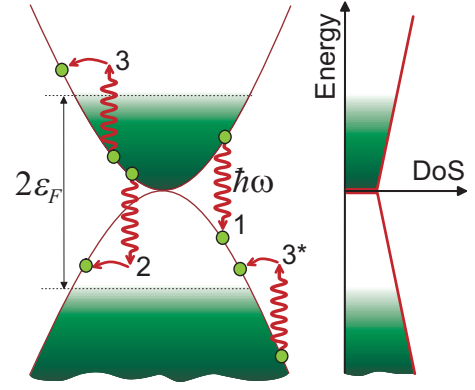


FIG. 2: Energy band diagram of a pumped GBL (left panel) and energy dependency of its DoS (right panel). Arrows correspond to direct and indirect interband transitions with the photon emission (wavy arrow "1" and wavy + smooth arrows "2") as well as to indirect intraband transitions with the photon absorption in the conduction and valence bands (wavy + smooth arrows "3" and "3*", respectively).

pensated donors (with the density $\Sigma_{D,R}$) and acceptors (with the density $\Sigma_{A,R}$). Hence $\Sigma_{D,R} - \Sigma_{A,R} \simeq \Sigma_A$. We further assume that in these heterostructures, the RIL might comprise the clusterized acceptors and donors (with the correlated charge defects forming the charged clusters with the charge $Z_c e > e$ and the characteristic size l_c , where e is the electron charge). In the latter case, we assume that the cluster density is equal to $(\Sigma_{A,R} + \Sigma_{D,R})/Z_c$. Such GBL-RIL heterostructures are quasi-neutral even in the absence of the pumping. Pumping results in the formation in the GBL of the two-dimensional (2D) electron and hole gases with the equal densities $\Sigma_e = \Sigma_h = \Sigma$ and the quasi-Fermi energies $\varepsilon_{F,e} = \varepsilon_{F,h} = \varepsilon_F$. Figure 2 shows the GBL band diagram under pumping. In Fig. 2, the arrows indicate different radiative transitions: vertical interband transitions, indirect intraband transitions accompanied by the electron scattering on the impurities, phonons, and holes (leading to the Drude absorption of radiation), and the interband indirect transitions.

The transverse electric field arising in the spacer due to the features of the doping can lead to the local opening of the energy gap [1, 34]. However, as shown below, for the doping levels under consideration, the energy gap expected to be small, and the band opening and the energy spectrum nonparabolicity will be disregarded [34–36]. The energy spectrum is assumed to be $\varepsilon_{\mathbf{p}} = \pm p^2 v_W^2 / \gamma_1 = \pm p^2 / 2m$, [1], where $\gamma_1 \simeq 0.35 - 0.43$ eV is the inter-GL overlap integral in GBLs, $v_W \simeq 10^8$ cm/s is the characteristic velocity, and $m = \gamma_1 / 2v_W^2$ is the effective mass of electrons and holes.

III. MAIN EQUATIONS

The real part of the net dynamic (THz) conductivity in the in-plane direction, $\text{Re } \sigma$, of GLs and GBLs comprises the contributions from the direct (vertical), $\text{Re } \sigma_d$, and two types of the indirect, $\text{Re } \sigma_{ind}^{inter}$ and $\text{Re } \sigma_{ind}^{intra}$, transitions, respectively:

$$\text{Re } \sigma = \text{Re } (\sigma_d + \sigma_{ind}^{inter} + \sigma_{ind}^{intra}). \quad (1)$$

The first term in Eq. (1) corresponds to the transitions of the type "1" in Fig.2, the second term corresponds to the type "2", and the third term - to the types "3" and "3*" transitions, respectively. The last term in the right-hand side of Eq. (1) corresponds to the processes responsible for the Drude absorption.

Due to high frequencies of the inter-carrier scattering under sufficiently strong pumping, the energy distributions of the pumped carriers are characterized by the Fermi distribution functions $f_v(\varepsilon_{\mathbf{p}})$ and $f_c(\varepsilon_{\mathbf{p}})$, where $\varepsilon_{\mathbf{p}}$ is the dispersion relationship for the 2D carriers in GBLs, with the quasi-Fermi energy, $\varepsilon_F \simeq \pi \hbar^2 \Sigma / 2m$ and the effective temperature T .

The calculations of the GBL dynamic conductivity in the in-plane direction associated with the direct inter-band transitions accounting for the GBL energy spectra, following the approach developed in [37, 38] (see, also [5]), yield:

$$\begin{aligned} \text{Re } \frac{\sigma_d}{\sigma_Q} &= \frac{(\hbar\omega + 2\gamma_1)}{(\hbar\omega + \gamma_1)} \tanh\left(\frac{\hbar\omega - 2\varepsilon_F}{4T}\right) \\ &\simeq 2 \tanh\left(\frac{\hbar\omega - 2\varepsilon_F}{4T}\right). \end{aligned} \quad (2)$$

Applying the Fermi golden rule for the indirect intra- and interband electron radiative transitions, we obtain at the following formulas for the respective components of the dynamic conductivity:

$$\begin{aligned} \text{Re } \frac{\sigma_{ind}^{intra}}{\sigma_Q} &= \frac{4\pi g}{\hbar\omega^3} \sum_{\mathbf{p}, \mathbf{p}'} |V(\mathbf{p} - \mathbf{p}')|^2 u_{\mathbf{p}\mathbf{p}'}^{\lambda\lambda'} (\mathbf{v}_{\mathbf{p}'} - \mathbf{v}_{\mathbf{p}})^2 \delta(\hbar\omega + \varepsilon_{\mathbf{p}} - \varepsilon_{\mathbf{p}'}) \\ &\times \left\{ \frac{1}{1 + \exp[(\varepsilon_{\mathbf{p}} - \varepsilon_F)/T]} - \frac{1}{1 + \exp[(\varepsilon_{\mathbf{p}'} - \varepsilon_F)]} \right\}, \end{aligned} \quad (3)$$

$$\begin{aligned} \text{Re } \frac{\sigma_{ind}^{inter}}{\sigma_Q} &= \frac{2\pi g}{\hbar\omega^3} \sum_{\mathbf{p}, \mathbf{p}'} |V(\mathbf{p} - \mathbf{p}')|^2 u_{\mathbf{p}\mathbf{p}'}^{cv} (\mathbf{v}_{\mathbf{p}'} + \mathbf{v}_{\mathbf{p}})^2 \delta(\hbar\omega - \varepsilon_{\mathbf{p}} - \varepsilon_{\mathbf{p}'}) \\ &\times \left\{ \frac{1}{1 + \exp[(\varepsilon_{\mathbf{p}} - \varepsilon_F)/T]} - \frac{1}{1 + \exp[(\varepsilon_{\mathbf{p}'} + \varepsilon_F)/T]} \right\}. \end{aligned} \quad (4)$$

Here $g = 4$ is the spin-valley degeneracy factor, $\varepsilon_{\mathbf{p}}$, $\mathbf{v}_{\mathbf{p}} = 2\mathbf{p}v_W^2/\gamma_1 = \mathbf{p}/m$ is the velocity of electrons and holes with the momentum \mathbf{p} in GBLs, $V(\mathbf{q})$ is the \mathbf{q} -the Fourier component of the scattering potential, $u_{\mathbf{p}\mathbf{p}'}^{\lambda\lambda'} = (1 + \lambda\lambda' \cos 2\theta_{\mathbf{p}\mathbf{p}'})/2$ is the overlap between the envelope wave functions in GBLs, and $\lambda = \pm 1$ is the index indicating the conduction and valence bands. The extra factor of 2 in Eq. (3) accounts for the intraband electron and hole contributions.

Equation (3) yields the well-known result for the dynamic Drude conductivity in the high-frequency limit $\Gamma = \hbar/\tau < \hbar\omega < \varepsilon_F$, where Γ is the broadening of the carrier spectra.

IV. SCATTERING MECHANISMS

For the GBL-RIL heterostructures under consideration, we have the following formulas:

$$|V(\hbar\mathbf{q})|^2 = \left[\frac{2\pi e^2}{\kappa(q + q_{TF})} \right]^2 [\Sigma_A + \Sigma_{RCL} \exp(-2qd)], \quad (5)$$

for the discrete acceptors in the GBL and the discrete acceptors and donors in the RIL and

$$\begin{aligned} |V(\hbar\mathbf{q})|^2 &= \left[\frac{2\pi e^2}{\kappa(q + q_{TF})} \right]^2 \\ &\times [\Sigma_A + Z_c \Sigma_{RCL} \exp(-2qd - q^2 l^2/2)], \end{aligned} \quad (6)$$

for the point charged defects (acceptors) in the GBL and the correlated clusterized acceptors and donors in the RIL, respectively. Here $q = |\mathbf{p} - \mathbf{p}'|$, $\Sigma_{RCL} = \Sigma_{A,R} + \Sigma_{D,R}$ is the net density of the charge impurities of both types located in the RIL (therefore the cluster density in the "clusterized" RIL is equal to Σ_{RCL}/Z_c with $\Sigma_{RCL} > \Sigma_A$), κ is the effective dielectric constant (which is the half-sum of the dielectric constants of the materials surrounding the GBL, i.e., of the spacer and the substrate), $q_{TF} = (4e^2 m / \hbar^2 \kappa)$ is the Thomas-Fermi screening wave number [38–40], which is independent of the carrier density. Deriving Eq. (6), we have taken into account that the density of the charged clusters in the clusterized RCL is Z_c -times smaller than the donor and acceptor densities, but the cross-section of the carrier scattering on the clusters is proportional to $Z_c^2 e^4$. The factor $\exp(-2qd)$ in Eqs. (5) and (6) is associated with the remote position of a portion of the charged scatterers (see, for example [31]). Equation (7) corresponds to the Gaussian spatial distributions of the clusters that leads to the appearance of the factor $\exp(-q^2 l^2/2)$ (compare with Refs. [29, 41–43]).

One can see that the scattering matrix element explicitly depends on the background dielectric constant κ and via the dependence of q_{TF} on κ .

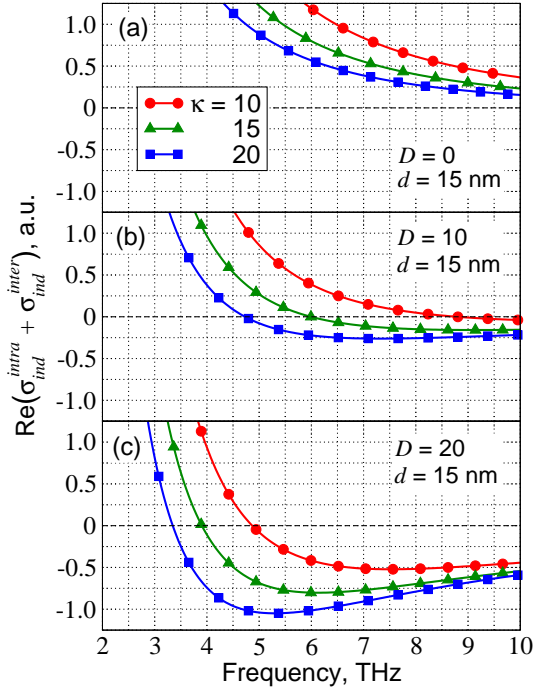


FIG. 3: Frequency dependences of $\text{Re}(\sigma_{ind}^{intra} + \sigma_{ind}^{inter})$ calculated for GBL-RIL heterostructures with spacer thickness $d = 15$ nm, different dielectric constants ($\kappa = 10, 15$, and 20), and different doping parameters D : (a) $D = 0$, (b) $D = 10$, and (c) $D = 20$.

V. NET THZ CONDUCTIVITY

In the following we consider the most practical case of the temperature, frequency range, and pumping in which $\hbar/\tau < \hbar\omega, T < \varepsilon_F$. For $T = 300$ K, the frequency range $\omega/2\pi = 1 - 10$ THz, and $\varepsilon_F \gtrsim 50$ meV, these inequalities are satisfied when $\tau \gtrsim 0.05 - 0.5$ ps.

For GBL structures without the RIL ($\Sigma_{RIL} = 0$) and the totally screened charges in the GBL, in which $\text{Re } \sigma_{ind}^{intra} = \overline{\sigma_{ind}^{intra}}$ and $\text{Re } \sigma_{ind}^{inter} = \overline{\sigma_{ind}^{inter}}$, invoking Eqs. (3) - (6), one obtains

$$\text{Re } \overline{\sigma_{ind}^{intra}} \simeq 2 \frac{e^2 \Sigma}{m\tau} \frac{1}{\omega^2} = 2\sigma_Q \left(\frac{\omega_D}{\omega} \right)^2, \quad (7)$$

where $\omega_D = \sqrt{4\hbar\Sigma/m\tau} = \sqrt{8\varepsilon_F/\pi\hbar\tau}$ is the Drude frequency. This quantity characterizes the relative strength of the Drude processes (absorption).

As the above takes place, Eqs. (3) and (4) lead to

$$\frac{\text{Re } \overline{\sigma_{ind}^{inter}}}{\text{Re } \overline{\sigma_{ind}^{intra}}} \simeq -\frac{\hbar\omega}{4\varepsilon_F}. \quad (8)$$

To avoid cumbersome calculations and obtain transparent formulas suitable for a qualitative analysis, we use the mean value theorem for the integrals over dq . As

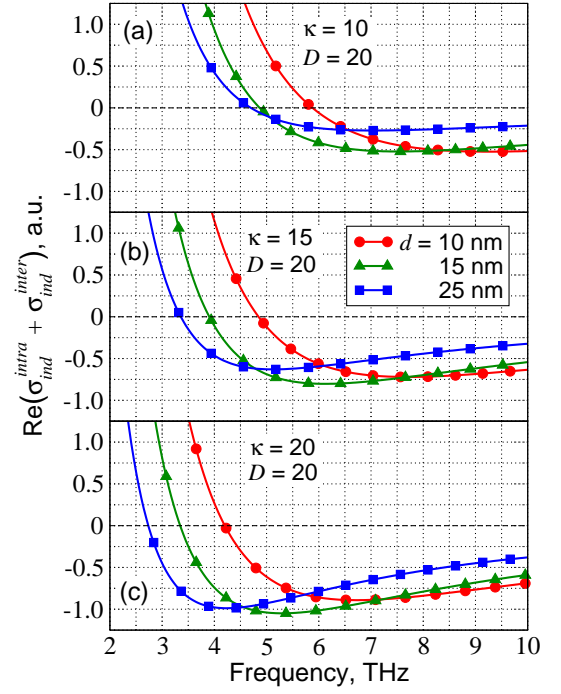


FIG. 4: The same as in Fig. 3 but for doping parameter $D = 20$, different spacer thicknesses ($d = 10, 15$, and 25 nm), and different dielectric constants: (a) $\kappa = 10$, (b) $\kappa = 15$, and (c) $\kappa = 20$.

a result, we arrive at the following simplified formulas for $\text{Re } \sigma_{ind}^{intra} + \text{Re } \sigma_{ind}^{inter}$:

$$\begin{aligned} & \text{Re } (\sigma_{ind}^{intra} + \sigma_{ind}^{inter}) \\ & \simeq \text{Re } \overline{\sigma_{ind}^{intra}} \left\{ \int_{Q_{min}}^{Q_{max}} dq q \frac{[1 + D \exp(-2qd - q^2 l^2/2)]}{(Q_{max}^2 - Q_{min}^2)(q/q_{TF} + 1)^2} \right. \\ & \quad \left. - \frac{\hbar\omega}{4\varepsilon_F} \int_{q_{min}}^{q_{max}} dq q \frac{[1 + D \exp(-2qd - q^2 l^2/2)]}{(q_{max}^2 - q_{min}^2)(q/q_{TF} + 1)^2} \right\}. \quad (9) \end{aligned}$$

Here $D = Z_c(\Sigma_{RCL}/\Sigma_A) = Z_c(\Sigma_{D,R} + \Sigma_{A,R})/(\Sigma_{D,R} - \Sigma_{A,R}) \simeq Z_c(\Sigma_{D,R} + \Sigma_{A,R})/\Sigma_A \geq Z_c \geq 1$ is the doping parameter ($Z_c = 1$ and $l = 0$ for the RGL with the point charges (acceptors and donors) and $Z_c > 1$ and $l = l_c$ in the case of RIL with the clustered acceptors and donors), $\hbar Q_{max} \simeq 2\sqrt{2m\varepsilon_F}(1 - \hbar\omega/4\varepsilon_F)$, $\hbar Q_{min} \simeq 2\sqrt{2m\varepsilon_F}(\hbar\omega/4\varepsilon_F)$, $\hbar q_{max} \simeq 2\sqrt{m\hbar\omega}$, $q_{min} \simeq 0$. The latter quantities follow from the conservation laws for the indirect intraband and interband radiative transitions. In particular, Eq. (9) gives rise to

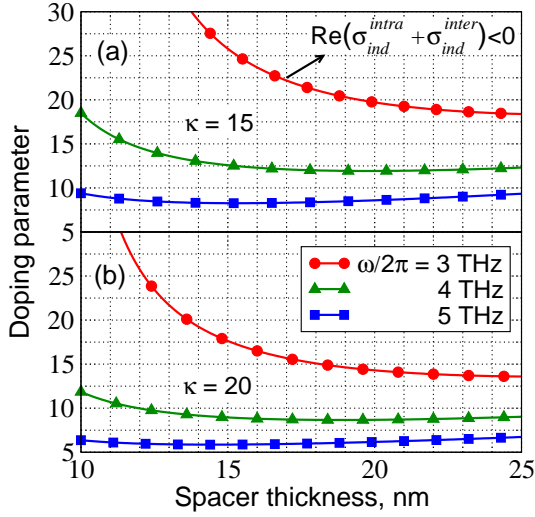


FIG. 5: Areas in the D - d plane where $\text{Re}(\sigma_{\text{ind}}^{\text{intra}} + \sigma_{\text{ind}}^{\text{inter}}) > 0$ (areas below lines corresponding to given frequencies) and $\text{Re}(\sigma_{\text{ind}}^{\text{intra}} + \sigma_{\text{ind}}^{\text{inter}}) < 0$ (above these lines) at different values of dielectric constant κ : (a) $\kappa = 15$ and (b) $\kappa = 20$.

$$\frac{\text{Re}(\sigma_{\text{ind}}^{\text{intra}} + \sigma_{\text{ind}}^{\text{inter}})}{\text{Re}\sigma_{\text{ind}}^{\text{intra}}} \simeq 1 - \frac{1}{2} \frac{\int_{q_{\min}}^{q_{\max}} dq q \frac{[1 + D \exp(-2qd - q^2 l^2/2)]}{(q/q_{TF} + 1)^2}}{\int_{Q_{\min}}^{Q_{\max}} dq q \frac{[1 + D \exp(-2qd - q^2 l^2/2)]}{(q/q_{TF} + 1)^2}}. \quad (10)$$

For sufficiently pure GBLs and relatively strong RIL doping (with nearly complete compensation of the donor and acceptors), the doping parameter parameters D can be fairly large. In this case, the contribution of the carrier scattering on the remote impurities to the net scattering rate can be dominant. In such a case, the absolute value of the net THz conductivity $|\text{Re}\sigma|$ can markedly exceed the contribution solely from the direct interband transitions, i.e., $|\text{Re}\sigma| > 2\sigma_Q$.

Considering Eqs. (1), (2), and (9), we arrive at the following formula for the net THz conductivity:

$$\frac{\text{Re} \sigma}{2\sigma_Q} \simeq \tanh\left(\frac{\hbar\omega - 2\varepsilon_F}{4T}\right) + \left(\frac{\omega_D}{\omega}\right)^2 \left\{ \int_{Q_{\min}}^{Q_{\max}} dq q \frac{[1 + D \exp(-2qd - q^2 l^2/2)]}{(Q_{\max}^2 - Q_{\min}^2)(q/q_{TF} + 1)^2} - \frac{\hbar\omega}{4\varepsilon_F} \int_{q_{\min}}^{q_{\max}} dq q \frac{[1 + D \exp(-2qd - q^2 l^2/2)]}{(q_{\max}^2 - q_{\min}^2)(q/q_{TF} + 1)^2} \right\}. \quad (11)$$

VI. RESULTS AND ANALYSIS

Using Eqs. (9) and (10), one can analyze the conditions when the interband radiative processes surpass the

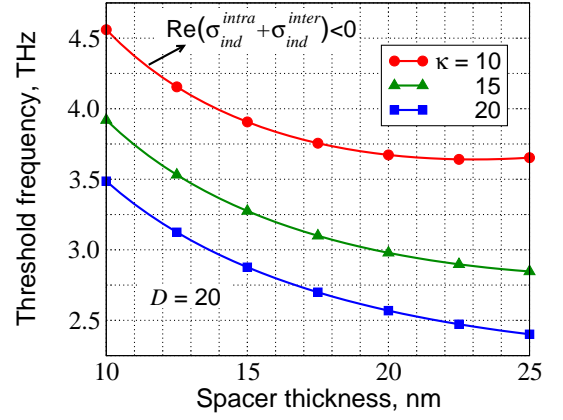


FIG. 6: Threshold frequency $\omega_0/2\pi$ corresponding to $\text{Re}(\sigma_{\text{ind}}^{\text{intra}} + \sigma_{\text{ind}}^{\text{inter}}) = 0$ as a function of the spacer thickness d calculated for $D = 20$ and different values of dielectric constant κ . AS in Fig. 5, areas above the pertinent line are related to $\text{Re}(\sigma_{\text{ind}}^{\text{intra}} + \sigma_{\text{ind}}^{\text{inter}}) < 0$.

intraband one's, i.e., when $\text{Re}(\sigma_{\text{ind}}^{\text{intra}} + \sigma_{\text{ind}}^{\text{inter}}) < 0$.

For the practical GBL-RIL heterostructures with the HfO_2 spacer and the substrate material like Si and SiC, the effective dielectric constant (which is the half-sum of the dielectric constants of the spacer and the substrate) is in the range $\kappa = 10 - 20$. In the calculations we assume set $m = 4 \times 10^{-29}$ g and $\varepsilon_F = 60$ meV ($\Sigma \sim 2.5 \times 10^{12}$ cm $^{-2}$).

Figures 3 and 4 show the dependences of $\text{Re}(\sigma_{\text{ind}}^{\text{intra}} + \sigma_{\text{ind}}^{\text{inter}})$ on the frequency $f = \omega/2\pi$ calculated using Eq. (9) with $l = 0$ (uncorrelated impurities in the RIL) for different values of the doping parameter D , the spacer thickness d , and effective dielectric constant κ . As seen from Fig. 3(a), in the absence of the RCL ($D = 0$), the indirect intraband transitions prevail over the indirect interband transitions. In such a case, the indirect transitions lead to the photon absorption in the entire frequency range, although the photon emission due to the interband transitions partially compensates the Drude absorption. This compensation is enhanced in the heterostructures with the doped RIL, i.e., for $D > 0$ [see Figs. 3(b) and 3(c)]: an increase in the doping parameter D leads to the appearance of the frequency range where $\text{Re}(\sigma_{\text{ind}}^{\text{intra}} + \sigma_{\text{ind}}^{\text{inter}}) < 0$. The latter range becomes wider (it starts from lower frequency) with increasing dielectric constant κ . These features of the transformation of the $\text{Re}(\sigma_{\text{ind}}^{\text{intra}} + \sigma_{\text{ind}}^{\text{inter}})$ frequency dependence are attributed to reinforcing of the long-range carrier scattering (with increasing D) and smoothing of the scattering potential (due to a stronger screening at higher κ). Both these effects result in an increase of the relative role of the indirect interband transitions. The scattering potential smoothing associated with an increase in the spacer thickness d also beneficial for the indirect interband transitions is seen in Fig. 4 as well.

Figure 5 shows the $D - d$ plane where $\text{Re}(\sigma_{\text{ind}}^{\text{intra}} + \sigma_{\text{ind}}^{\text{inter}}) > 0$ (below the D versus d lines) and $\text{Re}(\sigma_{\text{ind}}^{\text{intra}} + \sigma_{\text{ind}}^{\text{inter}}) < 0$ (above these lines).

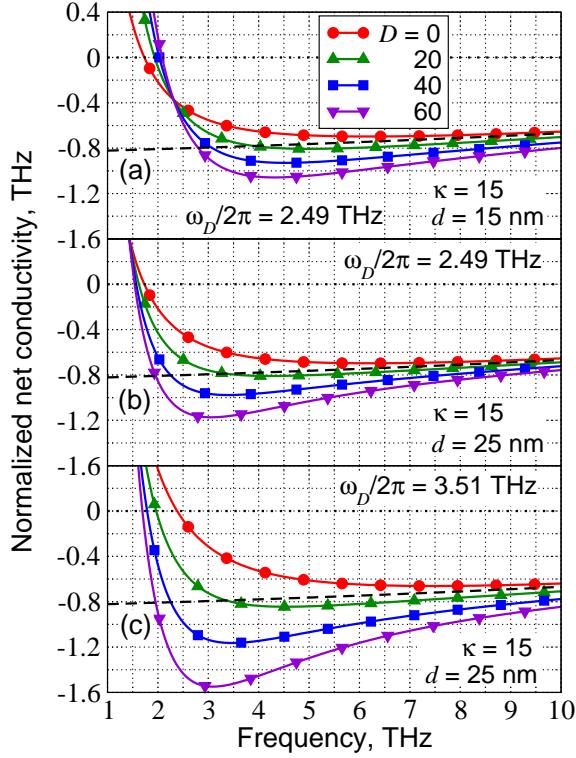


FIG. 7: Frequency dependence of the normalized net THz conductivity $\text{Re} \sigma / 2\sigma_Q$ of GBL-RIL heterostructures with $\kappa = 15$ and different values of doping parameter for: (a) $d = 15$ nm and $\omega_D/2\pi = 2.49$ THz ($\tau = 1$ ps), (b) $d = 25$ nm and $\omega_D/2\pi = 2.49$ THz ($\tau = 1$ ps), and (c) $d = 25$ nm and $\omega_D/2\pi = 3.51$ THz ($\tau = 0.5$ ps). Lines marked by circles correspond to normalize net THz conductivity without RIL ($D = 0$). Dashed lines show normalize THz conductivity due to solely direct interband transitions $\text{Re} \sigma_d / 2\sigma_Q$.

$\sigma_{ind}^{inter} < 0$ (above these lines) calculated considering Eq. (10) at different values of κ and frequency $f = \omega/2\pi$. As seen, the ranges of parameters D and d where the quantity $\text{Re} (\sigma_{ind}^{intra} + \sigma_{ind}^{inter})$ is negative are markedly wider in the case of relatively large dielectric constant κ and the frequency f .

Figure 6 shows the threshold frequency $\omega_0/2\pi$ corresponding to $\text{Re} (\sigma_{ind}^{intra} + \sigma_{ind}^{inter}) = 0$ as a function of the spacer thickness d calculated for $D = 20$ and different values of κ .

Figure 7 shows the frequency dependences of the normalized net THz conductivity $\text{Re} \sigma / 2\sigma_Q$ calculated using Eq. (11) for $T = 300$ K and different values of the doping parameter D , dielectric constant $\kappa = 15$, and Drude frequency $\Omega_D/2\pi$. The Drude frequencies are chosen to be $\omega_D/2\pi = 2.49$ and 3.51 THz. At $\varepsilon_F = 60$ meV, this corresponds to the carrier momentum relaxation time $\tau = 1$ ps and 0.5 ps, respectively. The latter values of τ corresponds to the carrier mobility in the GBL without the RIL, i.e., with $D = 0$, equal to $\mu = 40,000$ $\text{cm}^2/\text{V s}$ and $20,000$ $\text{cm}^2/\text{V s}$. The large values of D imply rather strong doping of the RIL. For

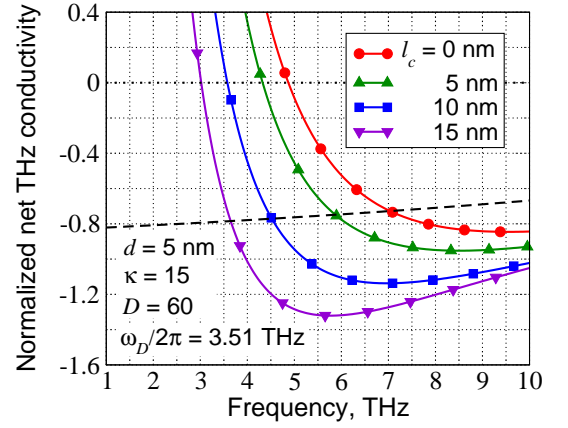


FIG. 8: Frequency dependence of the normalized net THz conductivity $\text{Re} \sigma / 2\sigma_Q$ of GBL-RIL heterostructures with clustered impurities, $\kappa = 15$, $\omega/2\pi = 3.51$ THz, $d = 15$ nm, $D = 60$, and different values of the cluster size l_c .

example, if $\Sigma_A = 1 \times 10^{11} \text{ cm}^{-2}$ (that is consistent with the above value of τ), the parameter D is equal to 60 if $\Sigma_{D,R} = 3.05 \times 10^{12} \text{ cm}^{-2}$ and $\Sigma_{D,R} = 2.95 \times 10^{12} \text{ cm}^{-2}$. g. As seen in Fig. 7, the net THz conductivity is negative in a certain range of frequencies (above 1.5 THz) even for the case $D = 0$, i.e., even in the GBL structures without the RIL. This is because although the indirect intraband transitions (Drude transitions) prevail over the indirect interband transitions, the negative contribution of the direct interband transitions enable the negativity of the net conductivity. The latter is because the contribution of the direct transitions decreases with increasing frequency much slowly (see the dashed line in Fig. 7) than the contribution due to the Drude processes. However, in the GBL-RIL heterostructures with sufficiently strong doping (large D) the absolute value of the net THz conductivity is pronouncedly larger than in the similar heterostructures without the RIL. Moreover, the substantial contribution of the indirect interband transition can result in $|\text{Re} \sigma|$ markedly exceeding its values $|\text{Re} \sigma_d|$ associated with solely direct interband transitions (see the curves for $D = 40$, and 60 and the dashed lines in Fig. 7) and even exceed the maximum value of the latter $2\sigma_Q$ (see the curve for $D = 60$). The comparison of the frequency dependences in Fig. 7 for $D = 0$ and $D = 60$ reveals that the RIL can provide a substantial increase in the absolute value of the THz conductivity [up to 4 - 6 times increase in the range $\omega/2\pi = 3 - 5$ THz, compare the curves for $D = 60$ and $D = 0$ in Fig. 7(c)] and, hence, the corresponding enhancement of the laser THz gain (for the parameters under consideration). Such an increase can be even more large at somewhat lower frequencies.

The comparison of Figs. 7(b) and 7(c) also demonstrates that at larger Drude frequencies, i.e., at shorter carrier momentum relaxation time τ (and the same parameter D), the sag of the net THz conductivity frequency dependences becomes deeper. This is attributed

to an increase of the intensity of the indirect processes (both intraband and interband) when τ decreases.

The plots in Fig. 8 were obtained using Eq. (11) with $l = l_c \neq 0$. Figure 8 shows the frequency dependences of the normalized net THz conductivity in the GBL-RIL heterostructures with clusterized (correlated) impurities in the RIL. As seen from Fig. 8, for relatively small spacer thickness ($d = 5$ nm), the clusterization leads to an additional enhancement of the indirect interband transitions, reinforcing the negative THz conductivity, particularly with an increasing cluster size. However, at relatively large spacer thicknesses ($d \gtrsim 10$ nm), an increase in the absolute value of the net THz conductivity with increasing size of the clusters is insignificant, since in this case, D is determined not only by the doping of the RIL but the cluster charge Z_c . This means that the chosen value $D = 60$ can correspond to different densities $\Sigma_{D,R}$ and $\Sigma_{A,R}$ depending on Z_c . The latter, in turn, depends of the degree of the compensation of donors by acceptors in the clusters.

VII. DISCUSSION

If the RIL doping does not compensate the acceptor system in the GBL, the electron and hole quasi-Fermi energies $\varepsilon_{F,e}$ and $\varepsilon_{F,h}$ are generally not equal to each other even in the pumping conditions. However, at sufficiently strong pumping when the density of the injected (or optically pumped) carriers $\Sigma > \Delta\Sigma = \Sigma_{D,A} - \Sigma_{D,A} - \Sigma_{D,A}$, Eqs. (2), (9), and (10) are still approximately valid until $\hbar\omega/2 < \min\{\varepsilon_{F,e}, \varepsilon_{F,h}\}$.

The above model disregarded the opening of the band gap in the GBL under the transverse electric field arising due to the impurity charges in the RIL and GBL. Despite a fairly complex pattern of the opening gap in GBLs by the electric field and doping [41, 42], the pertinent energy gap Δ_g can roughly be estimated in the manner as it was done in [35]. In the absence of the electron and hole injection from the side contacts, the carrier density in the GBL is rather small due to the compensation of the acceptor charges in the GBL and the donor and acceptor charges in the RIL (see, Sec.II). In this case, $\Delta_g \sim eE_\perp d_{GBL}$, where $E_\perp = 4\pi e\Sigma_A/\kappa$ is the transversal electric field created by the charged impurities and $d_{GBL} \simeq 0.36$ nm is the spacing between GLs in the GBL, so that $\Delta_g \sim 4\pi e^2\Sigma_A d_{GBL}/\kappa$. Under the pumping conditions, the 2D electron and hole gases partially screen the electric field in the GBL structure. As a result, one obtains $\Delta_g \sim eE_\perp d_{GBL}^{eff}$ with $d_{GBL}^{eff} < d_{GBL}$ [35]. Taking into account the screening of the transversal electric field E_\perp by both electron and hole components, we obtain the following estimate: $\Delta_g \sim 4\pi e^2\Sigma_A d_{GBL}/\kappa[1 + (8d_{GBL}/a_B)]$, where $a_B = \kappa\hbar^2/me^2$ is the Bohr radius. Assuming $a_B = 10 - 20$ nm and $\Sigma_A = (5 - 10) \times 10^{11} \text{ cm}^{-2}$, we obtain $\Delta_g \sim 1.5 - 5$ meV. These values are in line with those estimated in [35] and extracted from the experimental data [44, 45]. This esti-

mate validates our model

In the case of the clusterized charged impurities, the long range variations of the potential associated with the clusters lead to the variation of the band gap. The latter variations reinforce the electron and hole scattering on the clusters, but this effect is not really essential.

In Eqs. (3) and (4), we have disregarded the indirect radiative processes associated with electron-hole scattering in the GBL. The point is that the probability of such processes is proportional to $[2\pi e^2/\kappa(q + q_{TF})]^2 \Sigma\eta$, where (in the degenerated two-dimensional electron and hole gases), the factors $\eta < 1$ is the fraction of electrons and holes effectively participated in the scattering processes $\eta = T/\varepsilon_F$ at $\hbar\omega < T$, so that $\Sigma\eta \simeq \Sigma_T = 2mT/\pi\hbar^2$. The values of q_{TF} and $\Sigma\eta$ are independent of the electron and hole densities and, hence, of the pumping conditions. This is because of the virtually constant density of state. At room temperatures, the value of Σ_T can be of the order of or less than Σ_A and much smaller than Σ_{RIL} . In the former case, one needs to replace the quantity D in equations (9) and (10) by $D^* = D/(1 + 2\Sigma_T/\Sigma_A)$.

VIII. CONCLUSIONS

We proposed to use the GBL-RIL heterostructure with the population inversion due to the electron and hole injection as the active region of interband THz lasers and demonstrated that the incorporation of the RIL enables a substantial reinforcement of the effect of negative THz conductivity and the laser THz gain. This is associated with the domination of the indirect interband transitions in the GBL over the indirect intraband transitions (resulting in the Drude absorption) when the carrier scattering on a long-range potential prevails. As shown, the latter can be realized due to the remote doping and enhanced by the clusterization of impurities.

Using a simplified device model, we calculated the THz conductivity of the GBL-RIL heterostructures as function of the frequency for different structural parameters (dopant densities, spacer thickness, impurity cluster size, and the injected carrier momentum relaxation time). We found that the absolute value of the THz conductivity in the GBL-RIL heterostructures with a sufficiently highly doped RIL separated from the GBL by a spacer layer of properly chosen thickness can exceed in several times the pertinent value in the GBL-heterostructures without the RIL. Thus, the remotely doped GBL heterostructures can be of interest for applications as the active media in the THz lasers.

Acknowledgments

The authors are grateful to D. Svintsov and V. Vyurkov for useful discussions and information. The work was supported by the Japan Society for Promotion of Science (Grant-in-Aid for Specially Promoted

Research # 23000008) and by the Russian Scientific Foundation (Project #14-29-00277). The works at UB and RPI were supported by the US Air Force award #

FA9550-10-1-391 and by the US Army Research Laboratory Cooperative Research Agreement, respectively.

-
- [1] A. H. Castro Neto, F. Guinea, N. M. R. Peres, K.S. Novoselov, and A. K. Geim, The electronic properties of graphene, *Rev. Mod. Phys.* **81**, 109 (2009), <http://dx.doi.org/10.1103/RevModPhys.81.109>.
 - [2] V. Ryzhii, M. Ryzhii, and T. Otsuji, Negative dynamic conductivity of graphene with optical pumping, *J. Appl. Phys.* **101**, 083114-1-4 (2007), doi: 10.1063/1.2717566.
 - [3] M. Ryzhii and V. Ryzhii, Ryzhii, Injection and population inversion in electrically induced p-n junction in graphene with split gates, *Jpn. J. Appl. Phys.* **46**, L151 (2007), doi: 10.1143/JJAP.46.L151.
 - [4] V. Ryzhii, M. Ryzhii, V. Mitin, and T. Otsuji, Toward the creation of terahertz graphene injection laser, *J. Appl. Phys.* **110**, 094503-1-9 (2011), doi:10.1063/1.3657853.
 - [5] V. Ya. Aleshkin, A. A. Dubinov, and V. Ryzhii, Terahertz laser based on optically pumped graphene: model and feasibility of realization *JETP Lett.* **89**, 63(2009), doi: 10.1134/S0021364009020039.
 - [6] S. Boubanga-Tombet, S. Chan, A. Satou, T. Otsuji, and V. Ryzhii, Ultrafast carrier dynamics and terahertz emission in optically pumped graphene at room temperature, *Phys. Rev. B* **85**, 035443-1-6 (2012), doi:10.1103/PhysRevB.85.035443.
 - [7] T. Otsuji, S. Boubanga-Tombet, A. Satou, H. Fukidome, M. Suemitsu, E. Sano, V. Popov, M. Ryzhii, and V. Ryzhii, Graphene-based devices in terahertz science and technology, *J. Phys. D* **45**, 303001-1-9 (2012), doi:10.1088/0022-3727/45/30/303001.
 - [8] T. Li, L. Luo, M. Hupalo, J. Zhang, M. C. Tringides, J. Schmalian, and J. Wang, Femtosecond population inversion and stimulated emission of dense Dirac fermions in graphene, *Phys. Rev. Lett.* **108**, 167401-1-4 (2012), <http://dx.doi.org/10.1103/PhysRevLett.108.167401>.
 - [9] Y. Takatsuka, K. Takahagi, E. Sano, V. Ryzhii, and T. Otsuji, Gain enhancement in graphene terahertz amplifiers with resonant structures, *J. Appl. Phys.* **112**, 033103-1-4 (2012), <http://dx.doi.org/10.1063/1.4742998>.
 - [10] T. Watanabe, T. Fukushima, Y. Yabe, S.A. Boubanga Tombet, A. Satou, A.A. Dubinov, V. Ya Aleshkin, V. Mitin, V. Ryzhii, and T. Otsuji, The gain enhancement effect of surface plasmon polaritons on terahertz stimulated emission in optically pumped monolayer graphene, *New J. Phys.* **15**, 075003-1-11 (2013), doi:10.1088/1367-2630/15/7/075003.
 - [11] T. Winzer, E. Maric, and A. Knorr, Microscopic mechanism for transient population inversion and optical gain in graphene, *Phys. Rev. B* **87**, 165413-1-5 (2013), <http://dx.doi.org/10.1103/PhysRevB.87.165413>.
 - [12] I. Gierz, J.C. Petersen, M. Mitrano, C. Cacho, I.C. Edmond Turcu, E. Springate, A. Stöhr, A. Köhler, U. Starke, and A. Cavalleri, Snapshots of non-equilibrium Dirac carrier distributions in graphene, *Nat. Mater.* **12**, 1119 (2013), doi:10.1038/nmat3757.
 - [13] S. Kar, D.R. Mohapatra, E. Freysz, and A.K. Sood, Tuning photoinduced terahertz conductivity in monolayer graphene: Optical-pump terahertz-probe spectroscopy, *Phys. Rev. B* **90**, 165420 (2014), <http://dx.doi.org/10.1103/PhysRevB.90.165420>.
 - [14] T. Li, L. Luo, M. Hupalo, J. Zhang, M.C. Tringides, J. Schmalian, and J. Wang, Femtosecond population inversion and stimulated emission of dense Dirac fermions in graphene, *Phys. Rev. Lett.* **108**, 167401-1-4 (2012), <http://dx.doi.org/10.1103/PhysRevLett.108.167401>.
 - [15] R.R. Hartmann, J. Kono, and M.E. Portnoi, Terahertz science and technology of carbon nanomaterials, *Nanotechnology* **25**, 322001-1-16 (2014), doi:10.1088/0957-4484/25.
 - [16] T. Otsuji, S. Boubanga-Tombet, A. Satou, M. Suemitsu, and V. Ryzhii, Spectroscopy study on ultrafast carrier dynamics and terahertz amplified stimulated emission in optically pumped graphene, *J. Infrared Millimeter and Terahertz Waves*, **33**, 825 (2012), doi: 10.1007/s10762-012-9908-8.
 - [17] I. Gierz, M. Mitrano, J.C. Petersen, C. Cacho, I. C. E. Turcu, E. Springate, A. Stöhr, A. Köhler, U. Starke, and A. Cavalleri, Population Inversion in Monolayer and Bilayer Graphene, *J. Phys.: Cond. Mat.* **27**, 164204-1-5 (2015), doi:10.1088/0953-8984/27/16/164204.
 - [18] A. A. Dubinov, V. Ya. Aleshkin, M. Ryzhii, T. Otsuji, and V. Ryzhii, Terahertz laser with optically pumped graphene layers and Fabry-Perot resonator *Appl. Phys. Express* **2**, 092301-1-3 (2009).
 - [19] V. Ryzhii, M. Ryzhii, A. Satou, T. Otsuji, A. A. Dubinov, and V. Ya. Aleshkin, Feasibility of terahertz lasing in optically pumped epitaxial multiple graphene layer structures, *J. Appl. Phys.* **106**, 084507-1-6 (2009), doi:10.1063/1.3247541.
 - [20] V. Ryzhii, A. A. Dubinov, T. Otsuji, V. Mitin, and M. S. Shur, Terahertz lasers based on optically pumped multiple graphene structures with slot-line and dielectric waveguides, *J. Appl. Phys.* **107**, 054505-1-3 (2010), doi:10.1063/1.3327212.
 - [21] F. Rana, Graphene terahertz plasmon oscillator, *IEEE Trans. Nanotechnol.* **7**, 91 (2008), doi: 10.1109/TNANO.2007.910334.
 - [22] A. A. Dubinov, V. Ya. Aleshkin V. Mitin, T. Otsuji, and V. Ryzhii, Terahertz surface plasmons in optically pumped graphene structures, *J. Phys. Cond. Mat.* **23**, 145302-1-8 (2011), doi:1088/0953-8984/23/14/145302.
 - [23] V. V. Popov, O. V. Polischuk, A. R. Davoyan, V. Ryzhii, T. Otsuji, and M. S. Shur, Plasmonic terahertz lasing in an array of graphene nanocavities, *Phys. Rev. B* **86**, 195437-1-6 (2012), doi:10.1103/PhysRevB.86.195437.
 - [24] A. Tredicucci and M. S. Vitiello, Device concepts for graphene-based terahertz photonics, *IEEE J. Select Topics in Quant. Electron.* **20**, 8500109 (2014), doi: 10.1109/JSTQE.2013.2271692.
 - [25] H. C. Liu, C. Y. Song, A. J. SpringThorpe, and J. C. Cao, Terahertz quantum-well photodetector, *Appl. Phys. Lett.* **84**, 4068 (2004), doi: 10.1063/1.1751620.
 - [26] B. S. Williams, Terahertz quantum-cascade lasers, *Nat.*

- Photon. **1**, 517 (2007), doi:10.1038/nphoton.2007.166.
- [27] S. Kumar, Recent progress in terahertz quantum cascade lasers, IEEE J. Sel. Top. Quantum. Electron. **17**, 38 (2011), doi:10.1109/JSTQE.2010.2049735.
 - [28] D. Svintsov, V. Ryzhii, and T. Otsuji, Negative dynamic Drude conductivity in pumped graphene, Appl. Phys. Express **7**, 115101-1-4 (2014), doi: 10.7567/APEX.7.115101.
 - [29] D. Svintsov, T. Otsuji, V. Mitin, M. S. Shur, and V. Ryzhii, Negative terahertz conductivity in disordered graphene bilayers with population inversion, Appl. Phys. Lett. **106**, 113501-1-4 (2015), <http://dx.doi.org/10.1063/1.4915314>
 - [30] M. Shur, *Physics of Semiconductor Devices*(Prentice-Hall, New Jersey, 1990). ISBN 0-13-666496-2
 - [31] A. Shik, *Quantum Wells: Physics and Electronics of Two-Dimensional Systems*(World Scientific, Singapore, 1997), ISBN 981 02 3279 9.
 - [32] T. Stauber, G. Gomez-Santos, F. Javier Garcia de Abajo, Extraordinary absorption of decorated undoped graphene, Phys. Rev. Lett. **112**, 077401 (2014), <http://dx.doi.org/10.1103/PhysRevLett.112.077401>.
 - [33] G. Konstantatos, M. Badioli, L. Gaudreau, J. Osmond, M. Bernechea, F. P. Garcia de Arquer, F. Gatti, F. H. L. Koppens, Hybrid graphene quantum dot phototransistors with ultrahigh gain, Nature Nanotechnol. **7**, 363-368 (2012), doi:10.1038/nnano.2012.60
 - [34] E. McCann and V. Fal'ko, Landau-level degeneracy and quantum hall effect in a graphite bilayer, Phys. Rev. Lett. **96**, 0886805 (2006), <http://dx.doi.org/10.1103/PhysRevLett.96.086805>.
 - [35] E. McCann, D. S. L. Abergel, and V. I. Fal'ko, The low energy electronic band structure of bilayer. Eur. Phys. J. Special Topics **148**, 91- 103 (2007), doi: 10.1140/epjst/e2007-00229-1 .
 - [36] L. M. Zhang, Z. Q. Li, D. N. Basov, M. M. Fogler, Z. Hao, and M. C. Martin, Determination of the electronic structure of bilayer graphene from infrared spectroscopy Phys. Rev. B **78**, 235408-1-5 (2008), <http://dx.doi.org/10.1103/PhysRevB.78.235408>.
 - [37] L. A. Falkovsky and S. S. Pershoguba, Optical far-infrared properties of a graphene monolayer and multilayer, Phys. Rev. B **76**, 153410-1-4 (2007), <http://dx.doi.org/10.1103/PhysRevB.76.153410>.
 - [38] S. Das Sarma, E. H. Hwang, and E. Rossi, Theory of carrier transport in bilayer graphene Phys. Rev. B. **81**, 161407(R) (2010).doi: 10.1103/PhysRevB.81.161407
 - [39] E. McCann, M. Koshino, The electronic properties of bilayer graphene, Rep. Prog. Phys. **76**, 056503 (2013). doi: 10.1088/0034-4885/76/5/056503
 - [40] H. Min, D. S.L. Abergel, E. H. Hwang, and S. Das Sarma, Optical and transport gaps in gated bilayer graphene, Phys. Rev. B **84**, 041406-1-4(R) (2011), <http://dx.doi.org/10.1103/PhysRevB.84.041406>.
 - [41] F. T. Vasko and V. Ryzhii, Voltage and temperature dependencies of conductivity in gated graphene, Phys. Rev B **76**, 233404 (2007). <http://dx.doi.org/10.1103/PhysRevB.76.233404>.
 - [42] C. H. Lewenkopf, E. R. Mucciolo, and A. H. Castro Neto, Numerical studies of conductivity and Fano factor in disordered graphene Phys. Rev. B **77**, 081410(R) (2008). <http://dx.doi.org/10.1103/PhysRevB.77.081410>.
 - [43] S. Adams, P. W. Brouwer, and S. Das Sarma, Crossover from quantum to Boltzmann transport in graphene Phys. Rev. B **79**, 201404 (2009). <http://dx.doi.org/10.1103/PhysRevB.79.201404>.
 - [44] A. J. Samuels and J. D. Carey, Molecular Doping and Band-Gap Opening of Bilayer Graphene Alexander J. Samuels, and J. David Carey, ACS Nano, 2013, **7** (3), 2790 (2013). doi: 10.1021/nn400340q
 - [45] W. Zhang, Ch.-Te Lin, K.-Ku Liu, T. Tite, Ch.-Y. Su, Ch.-H. Chang, Yi-H. Lee, Ch.-W. Chu, K.-H. Wei, J.-L. Kuo, and L.-J. Li, Opening an electric band gap of bilayer graphene with molecular doping, ACS Nano **5** (9), 7517 (2011).doi: 10.1021/nn202463g